eScience xxx (xxxx) xxx

Contents lists available at ScienceDirect

eScience

journal homepage: www.keaipublishing.com/en/journals/escience

Ultrafine Cu nanoclusters confined within covalent organic frameworks for efficient electroreduction of CO_2 to CH_4 by synergistic strategy

Mi Zhang [a,1], Meng Lu [a,1], Ming-Yi Yang [a,1], Jia-Peng Liao [a], Yu-Fei Liu [a], Hao-Jun Yan [a], Jia-Nan Chang [b], Tao-Yuan Yu [b], Shun-Li Li [a], Ya-Qian Lan [a,*]

[a] School of Chemistry, South China Normal University, Guangzhou, 510006, PR China
[b] Jiangsu Collaborative Innovation Centre of Biomedical Functional Materials, School of Chemistry and Materials Science, Nanjing Normal University, Nanjing, 210023, PR China

HIGHLIGHTS

- A study on using the confinement effect of COFs to embed Cu nanoclusters for ECR to CH_4 with industrial current density.
- Cu-NC@CuPc-COF achieves a maximum CO_2-to-CH_4 FE of 74 ± 3% (at −1.0 V) with a j_{CH_4} of 538 ± 31 mA cm^{-2} (at −1.2 V).
- In situ FT-IR and DFT calculation shows that both Cu NCs and CuPc collaboratively contributes to high activity for ECR.

GRAPHICAL ABSTRACT

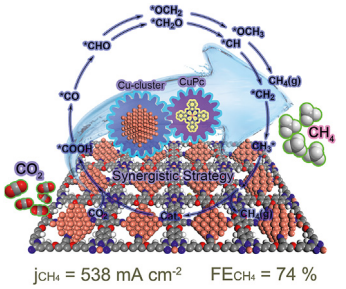

ARTICLE INFO

Keywords:
Covalent organic frameworks
Metal nanoclusters
CO_2 electroreduction

ABSTRACT

Electrocatalytic CO_2 reduction (ECR) to high value-added chemicals by using renewable electricity presents a promising strategy to realize "carbon neutrality". However, the ECR system is still limited by its low current density and poor CO_2 utilization efficiency. Herein, by using the confinement effect of covalent organic frameworks (COFs) to confine the *in-situ* growth of metal nanoclusters (NCs), we develop a series of Cu NCs encapsulated on COF catalysts (Cu-NC@COF) for ECR. Among them, Cu-NC@CuPc-COF as a gas diffusion electrode (GDE) achieves a maximum CO_2-to-CH_4 Faradaic efficiency of 74 ± 3% (at −1.0 V vs. Reversible Hydrogen Electrode (RHE)) with a current density of 538 ± 31 mA cm^{-2} (at −1.2 V vs. RHE) in a flow cell, making it one of the best among reported materials. More importantly, the current density is much higher than the relevant industrial current density (200 mA cm^{-2}), indicating the potential for industrial application. This work opens up new possibilities for the design of ECR catalysts that utilize synergistic strategy.

1. Introduction

The massive emission of carbon dioxide (CO_2) into the atmosphere due to the extensive use of fossil fuels has caused serious environmental problems, such as global warming and rising sea levels [1,2]. Many countries have proposed "carbon-neutral" strategies to mitigate these issues [3]. It is generally recognized that there are mainly two ways to reduce atmospheric CO_2 concentration: direct capture/storage and

* Corresponding author.
E-mail address: yqlan@m.scnu.edu.cn (Y.-Q. Lan).
[1] These authors contributed equally to this work.

https://doi.org/10.1016/j.esci.2023.100116
Received 29 November 2022; Received in revised form 5 February 2023; Accepted 27 February 2023
Available online xxxx

Please cite this article as: M. Zhang et al., Ultrafine Cu nanoclusters confined within covalent organic frameworks for efficient electroreduction of CO_2 to CH_4 by synergistic strategy, eScience, https://doi.org/10.1016/j.esci.2023.100116

chemical transformation/utilization [4]. Among these, the conversion of CO_2 into fuels or high value-added chemicals provides a more promising way to close the carbon cycle [5,6]. Electrocatalytic reduction of CO_2 is one of the effective methods to convert CO_2 into fuels and thus contribute to achieving carbon neutrality [7–9]. In recent years, various catalytic materials have been developed to accomplish this catalytic process, such as single-atom catalysts (SACs) [10,11], molecular catalysts [12,13], reticular materials (including metal–organic frameworks (MOFs), covalent organic frameworks (COFs), and so on) [14–16], and nanostructured materials (include metal nanoclusters (NCs) and nanoparticles (NPs)) [17]. However, it is still a great challenge to achieve high efficiency and high selectivity simultaneously [5]. Theoretically, an electrocatalyst that achieves efficient CO_2 electroreduction needs to meet the following features at the same time: 1) high CO_2 enrichment and diffusion ability; 2) efficient electron conductivity; 3) high catalytic site dispersion/utilization; and 4) high stability during the reaction process. Therefore, the rational design of catalyst materials that meet the above criteria is the first step toward realizing practical applications for CO_2 electroreduction.

Metal clusters, especially copper-based cluster catalysts, have shown high activity for the electrocatalytic reduction of CO_2 [5,18]. Metal clusters are promising catalysts for realizing high catalytic CO_2 reduction performance because their nanostructures can be designed and their size controlled. Furthermore, the multi-electron transfer properties of metal cluster-based catalysts enable them to accomplish the efficient conversion of CO_2 to various products. However, it is difficult to synthesize uniform metal nanoclusters, and they have stability issues, such as tending to aggregate during the catalytic process that greatly limit their practical application [19]. Using the confinement effect of porous supports to encapsulate metal NCs has proven to be an effective way of improving their stability during the reaction and also can suppress their aggregation or leaching under harsh reaction conditions [20]. Further, the porous environment of the supports regulates the metal NCs' geometric and electronic structures, making the catalyst more likely to exhibit enhanced activity and selectivity [21,22]. However, currently reported porous platforms, such as carbon materials (graphene, carbon nanotubes, etc.), inorganic materials (zeolites), and microporous crystalline supports (such as MOFs, hydrogen-bonded organic frameworks), often have difficulty satisfying the stability, uniformity, and porosity criteria simultaneously [23–25], and they have low designability and poor adjustability, limiting the applicability of the supported metal clusters. It is therefore vital to find a suitable porous platform to realize the above functionality [21,26].

Covalent organic frameworks (COFs) are an emerging class of porous crystalline materials with high structural stability, designability, and well-defined regular pore structures, making them promising platforms for uniformly supporting and encapsulating metal NCs [27–30]. Importantly, the isolated pores in COFs can prevent the aggregation of supported NCs and enable their uniform dispersion through the confinement effect, thus guaranteeing that they remain in their intrinsic active sites during the catalytic process [31–33]. In addition, strong interactions such as the coordinate bond between metal NCs and COF pores contribute to maintaining the structural stability of the confined NCs [32,34]. More importantly, functionalized COFs can also play a major role in catalytic CO_2 reduction, such as by enhancing CO_2 adsorption or using their intrinsic active sites to activate CO_2 [35,36]. Furthermore, the conductivity of two-dimensional (2D) COFs due to π-conjugation interactions ensures efficient electron transmission when they are used as electrocatalysts and catalyst supports. Therefore, confining metal NCs in functional COFs allows for synergy between the metal NCs and the functional sites in the backbones of COFs, thus effectively facilitating CO_2 utilization and conversion efficiency.

Based on the above factors, we rationally designed and synthesized a series of cyano-contained COFs to support ultrafine and highly dispersed Cu–NCs and used these composites (named Cu-NC@COF) as catalysts for highly effective ECR to CH_4. In the *in-situ* growth process, the coordination in COF pores guides the formation of ultrafine Cu NCs, and the confinement effect ensures their high dispersion and stability. As a result, based on porous Cu-phthalocyanine COF (CuPc-COF) as a platform, the Cu-NC@CuPc-COF catalyst achieves the highest FE (CH_4) of ~74 ± 3% (at −1.0 V vs. RHE) and a maximum current density of 538 ± 31 mA cm^{-2} (at −1.2 V vs. RHE), making it one of the best among reported catalysts. The conversion current density for CO_2 to CH_4 was superior to that of a state-of-the-art electrocatalyst and much higher than the commercially relevant current density (200 mA cm^{-2}), making the catalyst potentially useful for industrial applications. The *in-situ* Fourier transform infrared spectroscopy (FT-IR) and density functional theory (DFT) results showed that in the Cu-NC@CuPc-COF electrocatalyst, both Cu single clusters and Cu single sites in CuPc-COF provide highly active sites for CO_2-to-CH_4 conversion, thus contributing synergistic high activity and selectivity.

2. Materials and methods

2.1. Materials and synthetic procedures

All solvents and reagents obtained from commercial sources were used without further purification. 2,3,9,10,16,17,23,24-octahydroxyphthalocyaninato copper (CuPc-8OH, 95+%) was purchased from Shanghai Kylpharm Co., Ltd. Tetrafluorophthalonitrile (99%, TFPN) was purchased from Macklin/Aladdin (Shanghai). Triethylamine (99%, TEA), 1,4-dioxane, 1,3,5-trimethylbenzene, N,N-Dimethylformamide (DMF, AR), N,N-Dimethylacetamide (DMA, AR), and tetrahydrofuran (THF, 99.5%) were purchased from Sinopharm Chemical Reagent Co., Ltd.

2.2. Synthesis of COFs and Cu-NC@COFs

2.2.1. CuPc-COF

A Pyrex tube measuring 19 × 65 mm (o.d. × length) was charged with CuPc-8OH (35.2 mg, 0.05 mmol), TFPN (20 mg, 0.1 mmol), DMA (1.0 mL), and 1,3,5-trimethylbenzene (1.0 mL). After sonication for about 15 min to disperse evenly, 0.1 mL of TEA was added under shaking, then sonication was repeated for 5 min. After that, the tube was flash-frozen at 77 K (liquid N_2 bath) and degassed through three freeze–pump–thaw cycles by evacuation through an oil pump, then sealed under vacuum. After warming to room temperature, the mixture was heated at 150 °C and left undisturbed for 120 h. A black precipitate was isolated by filtration in a Buchner funnel through filter paper with an aperture of 0.25 μm and was washed with DMA, DMF, H_2O, CH_2Cl_2, and THF until the filtrate was colorless. The powder sample was then transferred to a Soxhlet extractor and washed with THF (24 h) and acetone (24 h). Finally, the product was evacuated at 120 °C under dynamic vacuum overnight to yield activated samples.

2.2.2. HHTP-COF (COF-316)

HHTP-COF was synthesized via a previously reported method [37]. HHTP (30 mg, 0.09 mmol), TFPN (27.6 mg, 0.138 mmol), 1,4-dioxane (2 mL), and TEA (0.078 mL) were mixed in a 19 × 65 mm Pyrex tube (o.d. × length). After sonication for about 15 min, the tube was flash-frozen at 77 K (liquid N_2 bath), degassed to achieve an internal pressure of ~100 mtorr, and sealed. Once it had warmed to room temperature, the mixture was heated at 120 °C and left undisturbed for 72 h. After filtration and washing with DMF, H_2O, and THF, the wet sample was transferred to a Soxhlet extractor and washed with THF (24 h) and acetone (24 h). Finally, the product was evacuated at 120 °C under dynamic vacuum overnight to yield activated samples in the form of a yellow powder.

2.2.3. Cu-NC@CuPc-COF

In a typical procedure, the as-prepared CuPc-COF (30 mg) was well dispersed in H_2O by sonication for 10 min, then 0.1 mL of 2 M $Cu(ClO_4)_2{\cdot}6H_2O$ was added, and the mixture was sonicated for another

10 min. It was then heated to 80 °C under an Ar atmosphere and stirred continuously for 10 h. The resulting solid was collected through centrifugation, then redisperse in a mixture of H_2O (9 mL) and hydrazine hydrate (1 mL) and stirred at 80 °C for 3 h under Ar to reduce Cu (II) to Cu (0). The Cu-NC@CuPc-COF was obtained by centrifugation, washed with H_2O (3 × 100 mL), and stored in an Ar atmosphere.

2.2.4. Cu-NC@HHTP-COF

The synthesis of Cu-NC@HHTP-COF was carried out by utilizing the same protocol for Cu-NC@CuPc-COF but starting with HHTP-COF (30 mg).

3. Results and discussion

3.1. Design and synthesis of COFs and Cu-NC@COFs

As shown in Scheme 1, in the first step of synthesizing the Cu-NC@COF, an aromatic nucleophilic substitution between *o*-difluorobenzene and catechol under the catalysis of triethylamine (TEA) was applied to condense 2,3,9,10,16,17,23,24-octahydroxyphthalocyaninato copper (CuPc) or triangular 2,3,6,7,10,11-hexahydroxytriphenylene (HHTP) with tetrafluorophthalonitrile (TFPN) to form two porous 2D COFs, named CuPc-COF and HHTP-COF (also known as COF-316). After that, two subnanometric Cu nanocluster confined COF composites (named Cu-NC@CuPc-COF and Cu-NC@HHTP-COF) were synthesized by *in-situ* impregnation–reduction routes. Specifically, the reduction of Cu (II) ion to Cu NCs was performed by introducing hydrazine hydrate ($N_2H_4{\cdot}xH_2O$) into the mixture through a hydrothermal method, with the –CN–Cu coordination interaction in the COF pores playing an important role in guiding the formation of well-defined Cu–NCs. It should be noted that Cu-NC@COF is sensitive to air and should be stored in Ar.

The crystalline structures of CuPc-COF, HHTP-COF, and Cu-NC@CuPc-COF/HHTP-COF were first studied by powder X-ray diffraction (PXRD). The results showed that the PXRD patterns of the as-synthesized COFs were good matches with the simulated patterns, and the sharp diffraction peaks demonstrated the samples' high crystallinity (Figs. 1a and b). The strong peaks at 4.37° for CuPc-COF and 4.47° for HHTP-COF were related to the (100) facet of the COFs [37–39]. However, a peak at the (100) facet of two COFs became relatively weak after the introduction of Cu clusters, which can be ascribed to the partial loss of a long-range order structure [32].

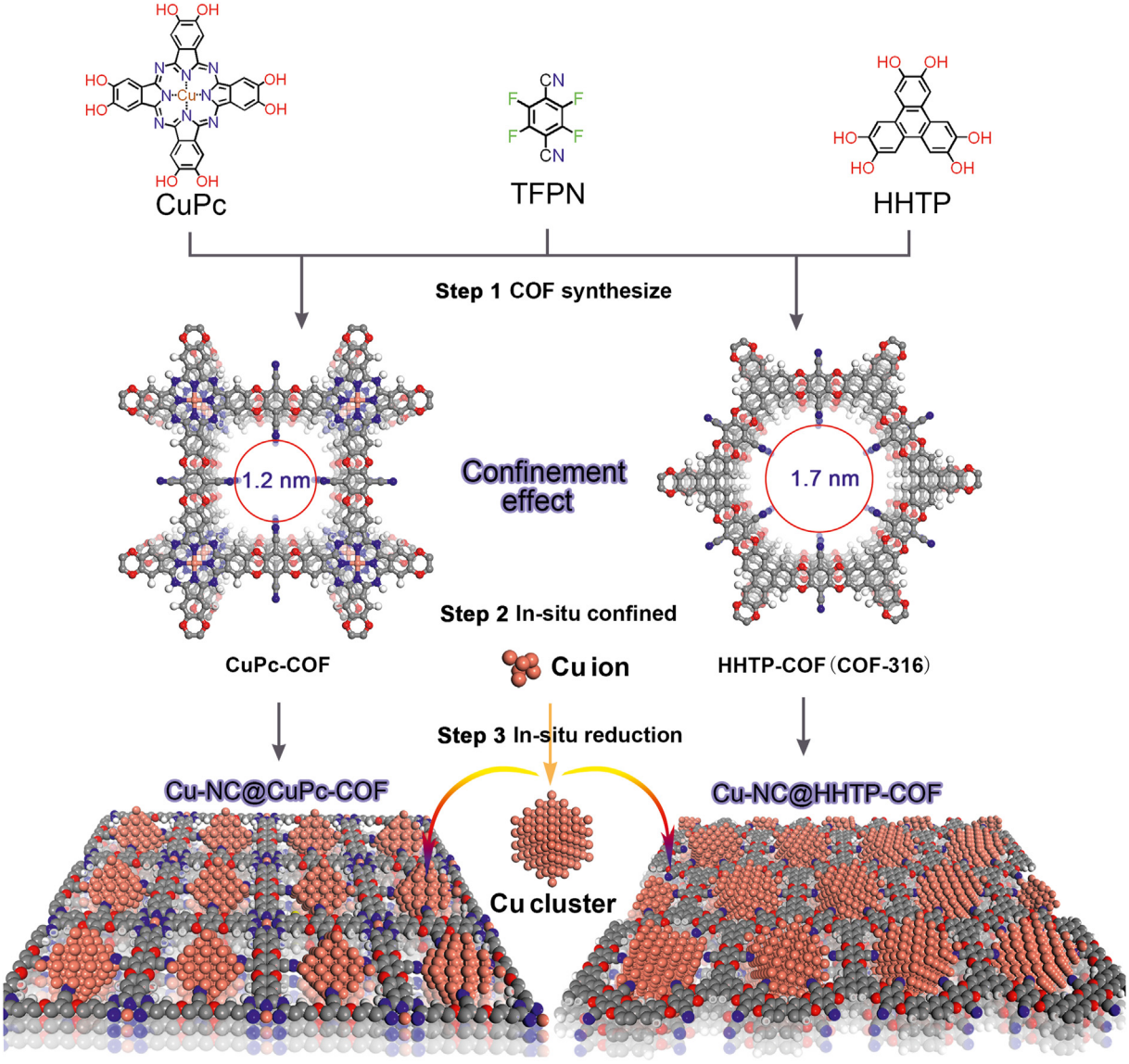

Scheme 1. Synthesis and structure illustrations of CuPc-COF, HHTP-COF, and the *in situ* confined process of Cu-NC in COFs to generate Cu-NC@CuPc-COF and Cu-NC@HHTP-COF.

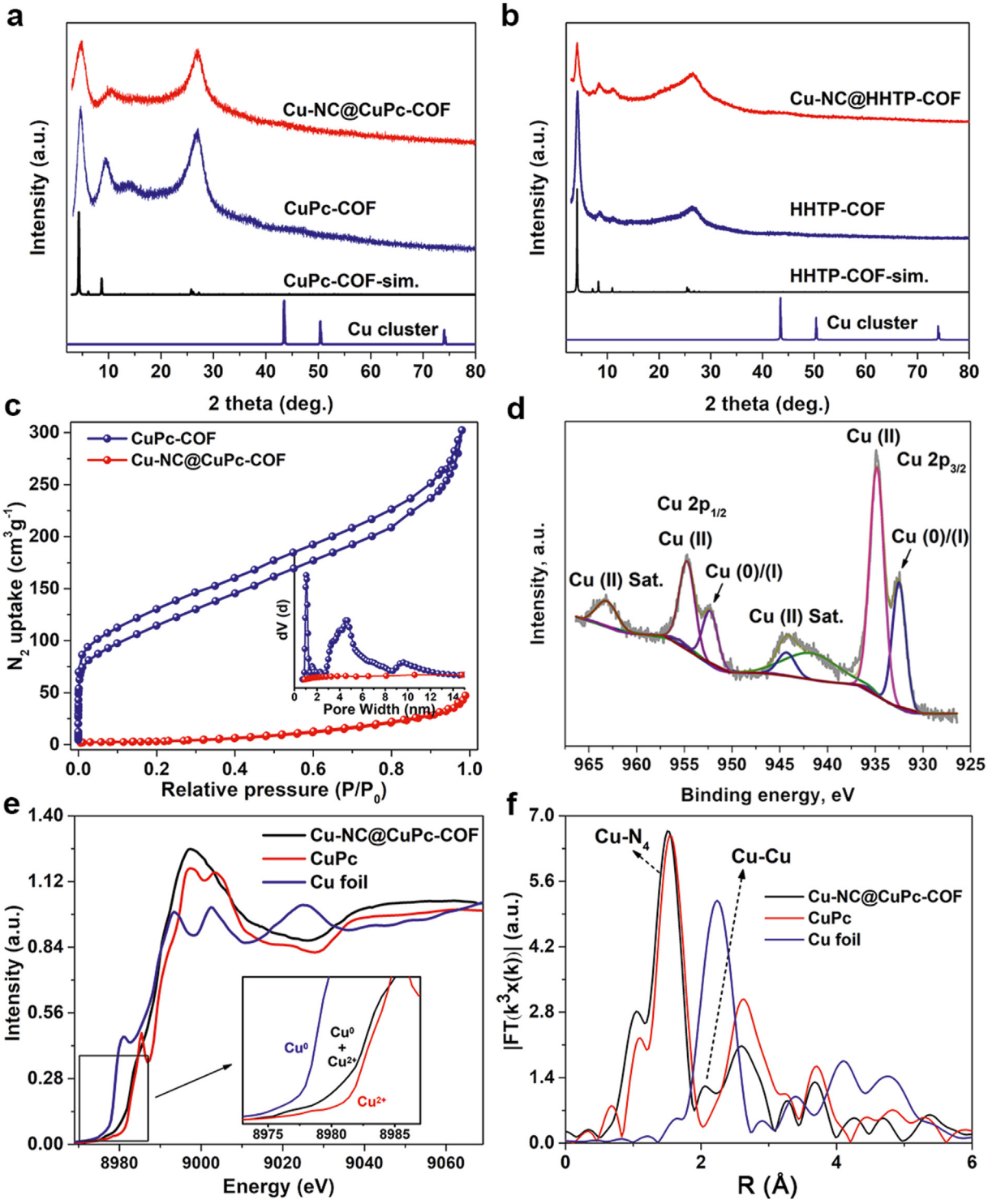

Fig. 1. Characterization of COFs and Cu-NC@COFs. (a) PXRD patterns of CuPc-COF and Cu-NC@CuPc-COF. (b) PXRD patterns of HHTP-COF and Cu-NC@HHTP-COF. (c) N_2 sorption isotherms and pore size distributions of CuPc-COF and Cu-NC@CuPc-COF. (d) High-resolution Cu 2p XPS spectra of Cu-NC@CuPc-COF. (e) Normalized Cu K-edge XANES and (f) FT-EXAFS spectra of Cu-NC@CuPc-COF, CuPc, and Cu foil.

Notably, no obvious diffraction peaks of Cu clusters were detected in Cu-NC@COFs, which is attributed to the ultrasmall sizes and high dispersion of the Cu clusters embedded in the COF [20].

The chemical structures, especially the formation of dioxin bonds in the COFs, were confirmed by FT-IR, which showed the characteristic –C–O asymmetric and symmetric stretching vibration bands at 1277 and 1010 cm^{-1}, also found in Cu-NC@COFs (Supporting Information Figs. S1 and S2). The porosity and surface areas of these COFs and Cu-NC@COFs were studied by nitrogen adsorption/desorption analysis at 77 K, the results of which showed that Cu-NC@COFs experienced an obvious reduction in surface area compared to raw COFs, according to Fig. 1c and Supporting Information Figs. S3–S6. This was due to pore blockage and the mass contribution of non-porous Cu–NCs. As expected, the pore size of Cu-NC@COFs was less than that of intrinsic COFs, as seen from the pore size distribution curves; this was because the slow diffusion kinetics of the Cu reduction reaction meant the Cu clusters formed in the early

stage occupied or blocked the entrance of 1D tunnels (pores) in the 2D COF crystal. This phenomenon is also attributed to the steric hindrance effect: that is, in a straight channel of the 2D COF, the Cu cluster that occupied the pores on the near-surface blocked the subsequent reaction, resulting in a decrease in the tested N_2 adsorption, thus causing largely low pore volume in the microporous region and low overall specific surface area. These results suggested that the COF pores were successfully occupied by Cu NCs of approximately the same size.

We then performed X-ray photoelectron spectroscopy (XPS) and obtained Cu LMM Auger spectra to study the Cu valence states in Cu-NC@COFs. In the XPS spectrum of Cu 2p for Cu-NC@CuPc-COFs (Figs. 1d and S7–9), the peaks at 934.7 and 932.5 eV (Cu $2p_{3/2}$) and at 954.7 and 952.3 eV (Cu $2p_{1/2}$), and the Cu LMM Auger peak at 918.6 eV correspond to Cu (II) and Cu (0) coexisting in Cu-NC@CuPc-COF. For Cu-NC@HHTP-COF, only Cu (0) was determined from the XPS and Cu LMM Auger spectra (Figs. S10–S12). The chemical state and local coordination environment of the Cu site within Cu-NC@COFs were further studied using Cu K-edge X-ray absorption fine structure (XAFS). In the normalized Cu K-edge XANES, compared to the standard CuPc and Cu foil samples (Fig. 1e) with their characteristic peak at ~8980 eV, the Cu-NC@CuPc-COF showed an obvious shift of the peak toward the lower energy side. This peak shift possibly suggests the appearance of the lower oxidation states Cu (0) or Cu (I) [40]. The Fourier transform (FT) k3-weighted EXAFS spectra of Cu-NC@CuPc-COF showed obvious peaks of Cu–N and Cu–Cu coordination, in contrast to the reference CuPc and Cu foil samples. These results further proved the existence of Cu NCs and CuPc in Cu-NC@CuPc-COF (Fig. 1f).

We then performed scanning electron microscopy (SEM), transmission electron microscopy (TEM), and high-angle annular dark-field scanning transmission electron microscopy (HAADF-STEM) to characterize the morphologies of the COFs and Cu-NC@COFs. The SEM images show that the surface morphologies of CuPc-COF/HHTP-COF and Cu-NC@CuPc-COF/Cu-NC@HHTP-COF were almost the same (Figs. S13 and S15). No large nanoparticles were observed on the surface of Cu-NC@COFs (Figs. 2a, 2b, S14 and S16). Energy-dispersive X-ray mapping revealed that Cu element was uniformly distributed on the CuPc-COF and HHTP COF (Figs. S17 and S18).

To further investigate the form of the Cu NCs, we then performed high-resolution TEM (HR-TEM) measurements. The images showed that the as-synthesized Cu-NC@COF possessed ultrasmall Cu NCs uniformly distributed on the COF supports (black dots at the center of black circles in Figs. 2c and d). The lattice spacing of Cu-NC was found to be ~0.2 nm, which could be indexed to the (111) planes of the Cu cluster (insets in Figs. 2e and f; note that relatively larger Cu clusters were selected to

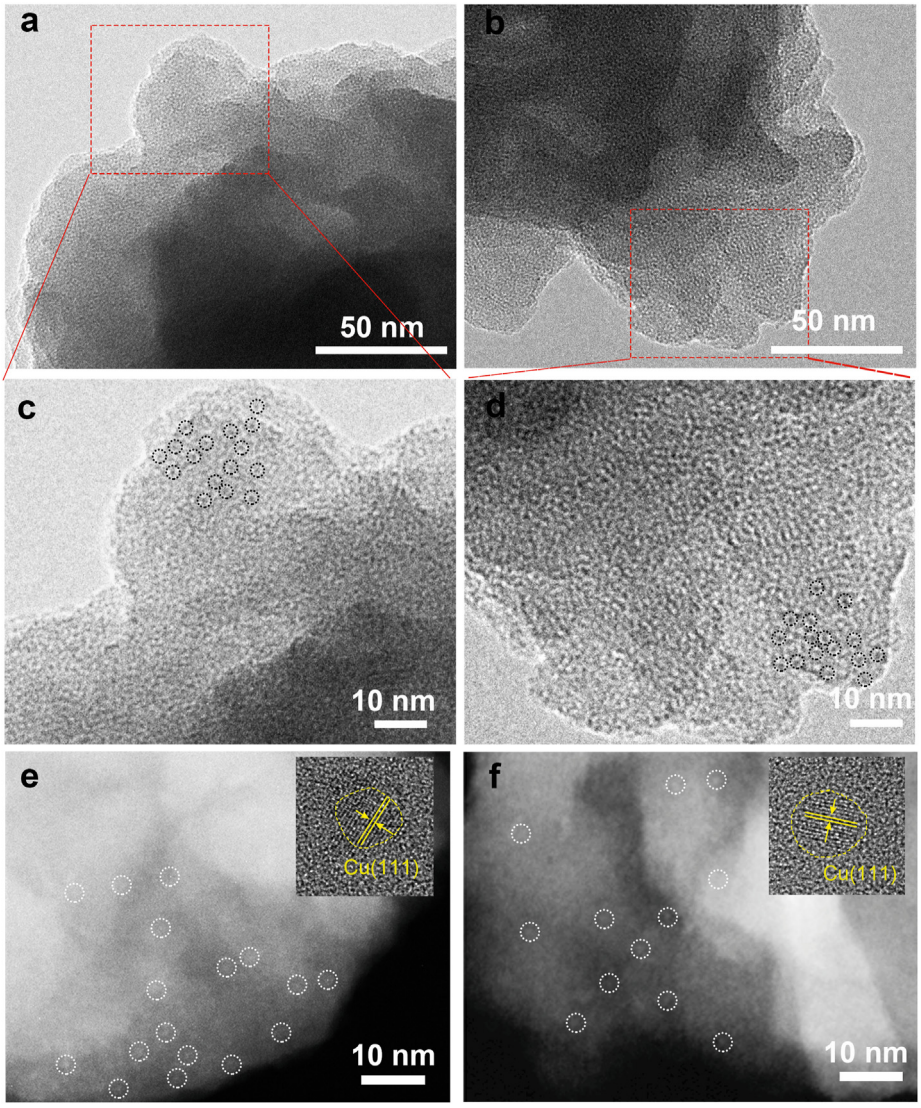

Fig. 2. Morphology analysis. TEM (a, b) and HR-TEM (c, d) images and HAADF-STEM (e, f) images of Cu-NC@CuPc-COF and Cu-NC@HHTP-COF. Insets in e and f show the lattice fringe of Cu–NCs. Note: The partial Cu nanoclusters are marked by black or white circles.

accurately determine the lattice fringes). The HAADF-STEM images also confirm that most of the Cu species were in ultrafine nanocluster form, represented as bright dots in the center of white circles. As shown in the size distribution curves in Fig. S19, the average size of the Cu NCs in Cu-NC@CuPc-COF and Cu-NC@HHTP-COF was found to be ~1.2 and ~1.7 nm, respectively, which approximately matched the pore sizes of CuPc-COF and HHTP COF. The content of Cu NCs in Cu-NC@COFs was studied by inductively coupled plasma (ICP) and thermo-gravimetric (TG) analysis (Figs. S20 and S21), which showed the overall mass content of Cu NCs to be ~8.3 and ~6.6 wt% in Cu-NC@CuPc-COF and Cu-NC@HHTP-COF, respectively.

3.2. ECR activity of COFs and Cu-NC@COFs

Based on the above characterizations of the structures and morphologies, it can be concluded that both Cu-NC@CuPc-COF and Cu-NC@HHTP-COF possess very uniformly dispersed Cu nanoclusters in COFs platforms. We studied their ECR activities as catalysts in a two-compartment flow-cell reactor (separated by Nafion 117 membrane) with 1.0 M KOH as the electrolyte. It is recognized that the current density (j) and Faradaic efficiency (FE) of the CO_2 reduction products are the two most important parameters for evaluating the activity of ECR catalysts [41]. As revealed in the linear sweep voltammetry (LSV) curves of CuPc-COF, Cu-NC@CuPc-COF, and Cu-NC@HHTP-COF (Fig. 3a), the Cu-NC@CuPc-COF showed notably enhanced current density as the applied potential increased, indicating it may have the highest electrocatalytic activity.

We then investigated in detail the FE of CO_2 to CH_4 by testing all the samples under potentials of −0.7 to −1.2 V vs. RHE (Fig. 3b). Interestingly, at all the applied potentials, the Cu-NC@CuPc-COF catalyst displayed superior performance to the CuPc-COF and much better performance than the Cu-NC@HHTP-COF, showing the superiority of the synergistic tandem action of the Cu NC and CuPc-COF. In the structure of Cu-NC@CuPc-COF, both the Cu NC and the CuPc acted as active sites for CO_2 electroreduction. However, Cu-NC@HHTP-COF contained only Cu NCs as active sites for electrocatalysis. Therefore, from a structural point of view, Cu-NC@CuPc-COF had a higher catalytic site utilization efficiency than Cu-NC@HHTP-COF and thus may show superior performance. In addition, the HHTP monomer in Cu-NC@HHTP-COF would have tended to engage in side reactions (the most likely competitor being H_2 evolution) due to the lack of active sites for CO_2 activation, thereby lowering the overall CO_2-to-CH_4 catalytic efficiency.

The highest FE (CH_4) values of Cu-NC@CuPc-COF, Cu-NC@HHTP-COF, and CuPc-COF were 74 ± 3%, 42 ± 2%, and 53 ± 2%, respectively. The FEs and ECR product distributions as a function of applied potentials from −0.7 to −1.2 V (vs. RHE) over COFs and Cu-NC@COFs are displayed in Figs. 3c and S22–S24. These show that the major products were CH_4 and the by-product H_2, along with minor amounts of C_2H_4 and CO. The source of the electrocatalytic products was analyzed via an isotope calibration experiment with gas chromatography and mass spectrometry (GC-MS). As displayed in Fig. 3d, we detected $^{13}CH_4$ ($m/z = 17$) and $^{12}CH_4$ ($m/z = 16$) in operating processes, proving that the produced CH_4 came from both the dissolved $^{13}CO_2$ and the HCO_3^- electrolyte solution. We then calculated the Tafel slopes to elucidate the kinetic activity of these catalysts for ECR (Fig. S25). The slopes were higher than 118 mV dec^{-1}, demonstrating that the rate-determining step (RDS) for the CO_2-to-CO* process was the adsorbed CO_2 receiving an electron and combining with H^+ from the electrolyte to form *COOH [42]. On the subsequent pathway to yield CH_4, it is generally believed that the RDS is the hydrogenation of *CO to *CHO [43–45].

The long-term stability of these catalysts was examined under a constant potential of −1.0 V vs. RHE (Figs. S26–S28). We found that Cu-NC@CuPc-COF could be continuously operated with a well-maintained high current density of ~236 ± 20 mA cm^{-2} and a stable FE (CH_4) of ~74 ± 2%, suggesting its stability for long-term operation. We also tested the long-cycling stability of the other two catalysts, which exhibited stable performance, as shown in the Supporting Information. After ECR testing, the morphology and composition of Cu-NC@CuPc-COF were intact, as confirmed by PXRD, HR-TEM, FTIR, and XPS results (Figs. S29–S33). Importantly, the Cu NCs still had their well-defined original size and high dispersion. All the above results indicate that the Cu-NC@COF possesses high stability in the reaction process, mainly due to the robust COF platform and the confinement effect of porous COFs, which prevent the agglomeration of the uniformly dispersed Cu NCs. However, the performance was not long enough to verify the stability of the material [46–48]. The chemical structures of our materials were intact after electrocatalytic testing, demonstrating the catalysts' chemical stability. These results suggested that our catalysts were not the intrinsic reason for the short durability. After in-depth exploration, we found that the most likely reason was a flooding phenomenon in our flow cell, which may have been due to the insufficient hydrophobicity of our catalyst, resulting in the electrolyte penetrating the active layer and suppressing contact between CO_2 and the catalyst [49].

A previously reported techno-economic model shows that a commercially feasible catalyst should be able to produce an industrially relevant current density for electrocatalysis to target products of over 200 mA cm^{-2} [50]. Fig. 3e shows the CO_2-to-CH_4 partial current densities of Cu-NC@CuPc-COF, Cu-NC@HHTP-COF, and CuPc-COF as catalysts at an applied potential of −0.7 V to −1.2 V vs. RHE. From the above results, we can conclude that the Cu-NC@CuPc-COF possessed the highest partial current density of 269 ± 24 mA cm^{-2} at −1.0 V vs. RHE, 391 ± 18 mA cm^{-2} at −1.1 V vs. RHE, and 538 ± 31 mA cm^{-2} at −1.2 V vs. RHE, much larger than the commercially relevant current densities, and also ranked above the most state-of-the-art catalysts reported for ECR to CH_4, as shown in a comparison of the partial current density of Cu-NC@CuPc-COF and many representative electrocatalysts (Fig. 3f). These results indicate the possibility for industrial application of this CO_2 electroreduction method to produce CH_4.

We then studied the reactive sites of the ECR reaction. For the catalytic reaction process, CO_2 molecules and solvent molecules must come into contact with active sites. For 2D materials such as those in this work, most of the catalytic processes take place on the [001] plane. In this study, the Cu NCs were uniformly distributed on the [001] plane and thus were used for CO_2 adsorption and the subsequent catalytic reaction.

An *in-situ* FT-IR test was then conducted to illustrate the CO_2 electroreduction mechanism for Cu-NC@COF catalysts (Figs. 4a, 4b and S34). According to previous studies, there are two main pathways for the electrocatalytic reduction of CO_2 to CH_4:

Path I: $*\rightarrow * + CO_2 \rightarrow *CO_2 \rightarrow *COOH \rightarrow *CO \rightarrow *CHO \rightarrow *OCH_2 \rightarrow *OCH_3 \rightarrow CH_4$

Path II: $*\rightarrow * + CO_2 \rightarrow *CO_2 \rightarrow *COOH \rightarrow *CO \rightarrow *CHO \rightarrow *CH_2O$ ($*C + H_2O$) $\rightarrow *CH \rightarrow *CH_2 \rightarrow *CH_3 \rightarrow CH_4$ [51,52]

In the *in-situ* electrochemical attenuated total reflection Fourier transform infrared (ATR-FTIR) spectra, the peaks at 1367 and 1597 cm^{-1} can be attributed to the symmetric and asymmetric OCO stretching of *COOH intermediate, and the peaks at 1229 and 1386 cm^{-1} belong to the C–OH stretching and the COO^- symmetric stretching, respectively, of *COOH, which is regarded as the key intermediate of CO_2 electroreduction [53–55]. The peaks at 1021 and 1180 cm^{-1} can be attributed to *CHO and *OCH_3, respectively, which are the crucial intermediates for CO_2-to-CH_4 Path I [56]. For clearer presentation, we enlarged the *in-situ* FT-IR spectrum (Fig. S35). As the electrolysis time increased, a positive band centered at ~2890 and 2920 cm^{-1} was observed and gradually increased with time, corresponding to the asymmetric *CH and *CH_2 species, which are the crucial intermediates for CO_2-to-CH_4 Path II [53,54,57].

The above results showed that the two reaction pathways for CO_2 to CH_4 coexist in the Cu-NC@ CuPc COF catalysts, corresponding to the two types of catalytic active sites (i.e., Cu atoms and Cu NCs) that result in the synergistic action of Cu-NC@ CuPc COF in the CO_2 reduction process. In detail, the CuPc in the composite material more efficiently generates

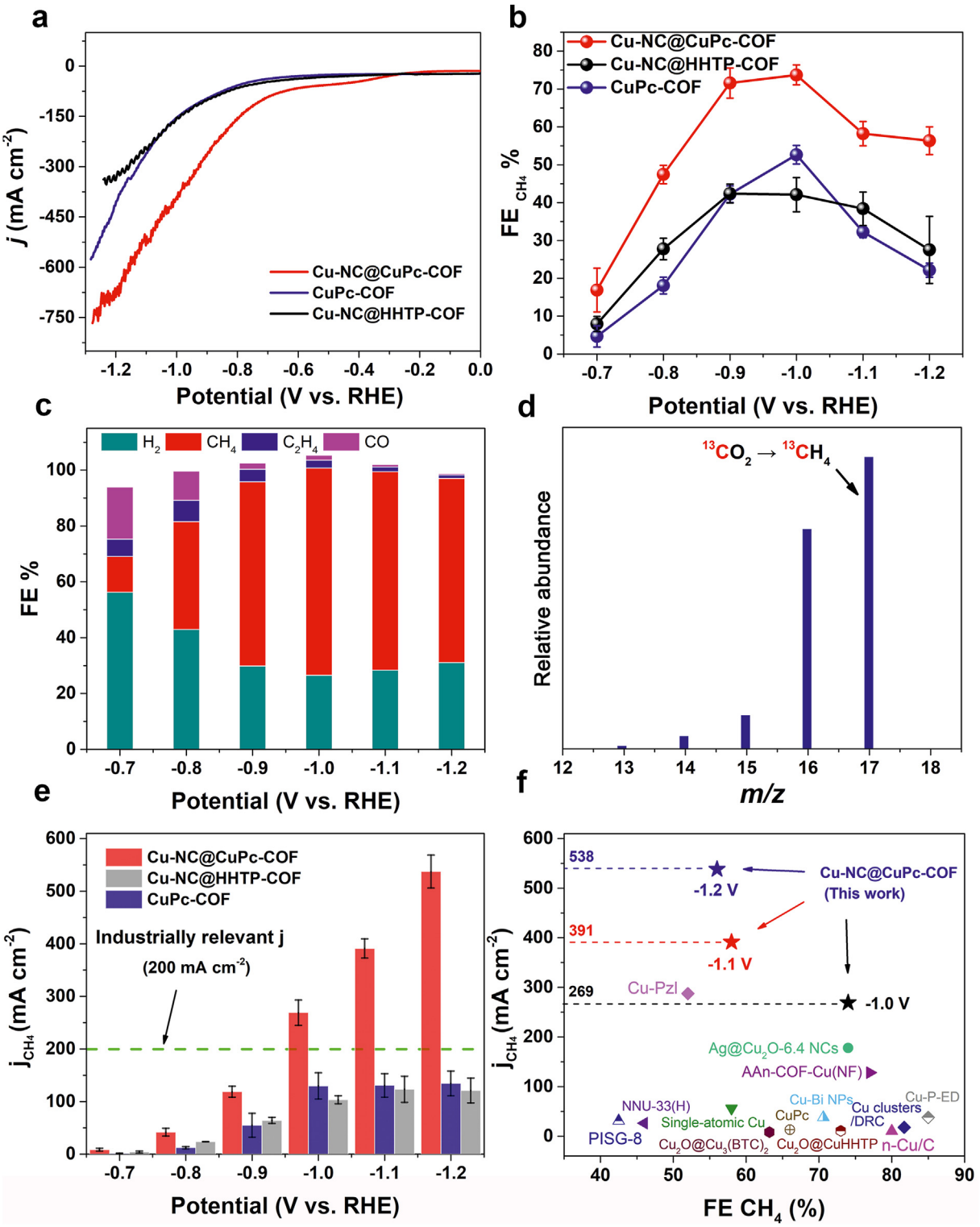

Fig. 3. Electrocatalytic CO_2 reduction performances of COFs and Cu-NC@COFs. (a) Linear sweep voltammetry curves. (b) The FE of CH_4 calculated over a potential range from −0.7 to −1.2 V vs RHE. (c) FE and the product distribution at different polarization potentials for Cu-NC@CuPc-COF. (d) The mass spectra of $^{13}CH_4$ recorded under a $^{13}CO_2$ atmosphere. (e) The partial current density distribution as a function of the potential for electroreduction of CO_2 to CH_4. (f) Comparison of the partial current density of CO_2 to CH_4 among Cu-NC@CuPc-COF and representative electrocatalysts.

*COOH and *CO intermediates (which are the two crucial intermediates for CO_2 reduction) and thus will increase the *COOH and *CO coverage concentration within the Cu-NC@CuPc-COF catalysts. We also calculated the free energy for the formation of intermediates *CO and *COOH on Cu-NC and CuPc-COF (Fig. S36). The results showed that the free energy of *CO_2 to *COOH and *CO was 1.982 and 0.725 eV for Cu clusters. However, the free energy of *CO_2 to *COOH and *CO was only 0.721 and 0.361 eV for CuPc-COF, much smaller than for Cu NCs. Therefore, the density functional theory (DFT) calculation results confirmed that the CuPc-COF generated *COOH and *CO more efficiently. The *COOH and *CO were then used for further steps to finally generate CH_4. This increased the overall CO_2 utilization and current density for Cu-

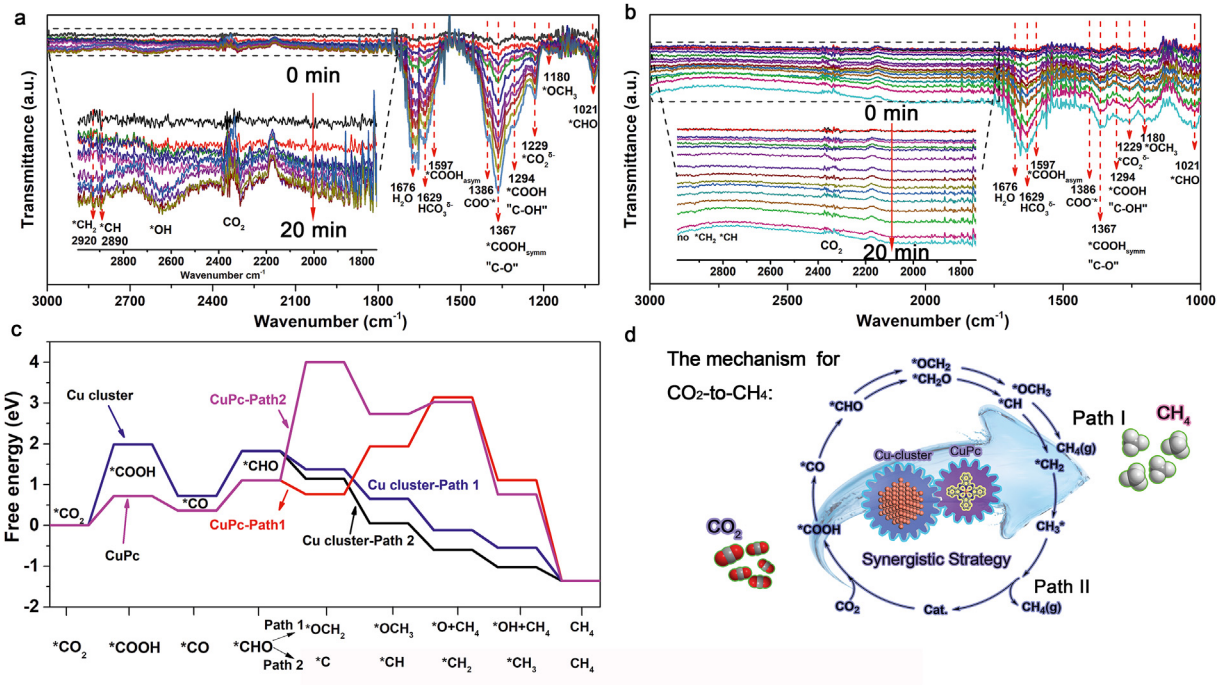

Fig. 4. The mechanism studies. *In situ* FT-IR spectrum of (a) Cu-NC@CuPc-COF and (b) CuPc-COF for the formation of CH_4, collected at −1.0 V vs. RHE in the flow cell. (c) The free-energy diagrams of CO_2 reduction to CH_4 for Cu NC and CuPc. (d) Proposed mechanism for the electrochemical reduction of CO_2 to CH_4.

NC@CuPc-COF compared to pure Cu NC and CuPc-COF (Figs. 3a and b). These results also explained why the performance of CuPc-COF with CuPc as active sites was better than that of Cu-NC@HHTP-COF with Cu NCs as active sites. Compared with the Cu clusters supported on a defect-rich carbon (DRC) reported previously [44], the single Cu sites only achieved the CO_2RR with a maximum ~22 mA cm^{-1}, much smaller than what the Cu-NC@CuPc-COF catalysts were capable of. These results proved the superiority of our dual-site synergistic materials.

We then conducted in situ infrared analysis of CuPc-COF samples; the results are shown in Fig. 4b. Two obvious peaks at 1021 and 1180 cm^{-1} appeared, corresponding to *CHO and *OCH_3, respectively, which are attributed to the two crucial intermediates for CO_2-to-CH_4 Path I. In contrast, the asymmetric *CH and *CH_2 species were not detected, thus ruling out Path II on CuPc-COF. We therefore confirmed that CH_4 generation occurred mainly through Path I in the CuPc-COF samples.

It is recognized that CH_x species tend to form on Cu (111) in Cu clusters/nanoparticles during the CO_2 electroreduction process [51]. We systematically calculated the free energy change of two sites for CO_2 reduction to CH_4. As shown in Fig. 4c, the key process to determine which path is taken is *CHO to *OCH_2 or to *C intermediate. The results showed that *CHO to *OCH_2 (Path I) behaves as an energy reduction process for CuPc, but *CHO to *C (Path II) needs a large Gibbs free energy of 2.2 eV, suggesting that CuPc sites are more conducive to Path I. For Cu clusters, although *CHO to *OCH_2 or *C both occurred spontaneously, the *CHO to *C process tended toward a smaller free energy (black curve), showing the Cu cluster sites were more conducive to Path II. In conclusion, all these results indicated that the electrocatalytic process of Path II occurs on the Cu NC of Cu-NC@CuPc-COF, while the process of Path I occurs on CuPc (Fig. 4d). These two active sites contribute the synergistic activity and selectivity for highly efficient CO_2 electroreduction to CH_4.

4. Conclusions

In summary, this work rationally designed a series of COF-confined Cu nanocluster composite catalysts that were used for the electrocatalytic reduction of CO_2 to CH_4 and yielded high conversion efficiency. As a result, Cu-NC@CuPc-COF achieved a Faradaic efficiency of ~74 ± 3% (at −1.0 V vs. RHE), along with a maximum current density of 538 ± 31 mA cm^{-2} (at −1.2 V vs. RHE) for CO_2 to CH_4 in a flow cell. More importantly, the CO_2-to-CH_4 conversion current density was much higher than these of most state-of-the-art electrocatalysts and matched or exceeded the commercially relevant current densities. The *in-situ* FT-IR results showed that in the Cu-NC@COF electrocatalysts, both Cu NCs and CuPc-COF play the role of active sites for CO_2-to-CH_4 conversion, thus contributing synergistic activity and selectivity. This work is a new example of using the confinement effect of pores to uniformly embed Cu nanoclusters into COFs for high-activity CO_2 electrochemical reduction. It also proves that designing electrocatalysts that utilize synergistic mechanisms can effectively improve catalytic activity, which opens up new opportunities in the development of electrocatalyst materials for practical applications.

Author contributions

Y. Q. Lan proposed the concept. M. Lu, M. Zhang, and all other co-authors performed the experiments. M. Zhang and M. Lu wrote the manuscript. All authors participated in data analysis and manuscript discussion.

Declaration of competing interest

The authors declare that they have no known competing financial interests or personal relationships that could have appeared to influence the work reported in this paper.

Acknowledgments

This work was financially supported by the NSFC (Nos. 22225109, 22071109, 22105080 and 22201083), the Project funded by the China Postdoctoral Science Foundation (Nos. 2020M682747 and 2021M701270), the Guangdong Basic and Applied Basic Research Foundation (Grant 2023A1515010779 and 2023A1515010928), the Guangzhou Basic and Applied Basic Research Fund Project (Grant

202102020209), China National Postdoctoral Program for Innovative Talents (BX20220115).

Appendix A. Supplementary data

Supplementary data to this article can be found online at https://doi.org/10.1016/j.esci.2023.100116.

References

[1] S. Solomon, G.-K. Plattner, R. Knutti, P. Friedlingstein, Irreversible climate change due to carbon dioxide emissions, P. Natl. Acad. Sci. 106 (2009) 1704.
[2] S.J. Davis, K. Caldeira, H.D. Matthews, Future CO_2 emissions and climate change from existing energy infrastructure, Science 329 (2010) 1330–1333.
[3] M. Zhou, T. Hu, Analysis of carbon emission status under the carbon neutral target in China for Earth's atmospheric balance, IOP Conf. Ser. Earth Environ. Sci. 804 (2021) 042082.
[4] O.S. Bushuyev, P. De Luna, C.T. Dinh, L. Tao, G. Saur, J. van de Lagemaat, et al., What should we make with CO_2 and how can we make it? Joule 2 (2018) 825–832.
[5] S. Nitopi, E. Bertheussen, S.B. Scott, X. Liu, A.K. Engstfeld, S. Horch, et al., Progress and perspectives of electrochemical CO_2 reduction on copper in aqueous electrolyte, Chem. Rev. 119 (2019) 7610–7672.
[6] S. Das, J. Pérez-Ramírez, J. Gong, N. Dewangan, K. Hidajat, B.C. Gates, S. Kawi, Core–shell structured catalysts for thermocatalytic, photocatalytic, and electrocatalytic conversion of CO_2, Chem. Soc. Rev. 49 (2020) 2937–3004.
[7] X. Wang, A. Xu, F. Li, S.-F. Hung, D.-H. Nam, C.M. Gabardo, et al., Efficient methane electrosynthesis enabled by tuning local CO_2 availability, J. Am. Chem. Soc. 142 (2020) 3525–3531.
[8] Y.Y. Birdja, E. Pérez-Gallent, M.C. Figueiredo, A.J. Göttle, F. Calle-Vallejo, M.T.M. Koper, Advances and challenges in understanding the electrocatalytic conversion of carbon dioxide to fuels, Nat. Energy 4 (2019) 732–745.
[9] D.H. Nam, P. De Luna, A. Rosas-Hernandez, A. Thevenon, F. Li, T. Agapie, et al., Molecular enhancement of heterogeneous CO_2 reduction, Nat. Mater. 19 (2020) 266–276.
[10] M. Li, H. Wang, W. Luo, P.C. Sherrell, J. Chen, J. Yang, Heterogeneous single-atom catalysts for electrochemical CO_2 reduction reaction, Adv. Mater. 32 (2020) 2001848.
[11] Y. Wang, Y. Liu, W. Liu, J. Wu, Q. Li, Q. Feng, et al., Regulating the coordination structure of metal single atoms for efficient electrocatalytic CO_2 reduction, Energy Environ. Sci. 13 (2020) 4609–4624.
[12] K. Elouarzaki, V. Kannan, V. Jose, H.S. Sabharwal, J.M. Lee, Recent trends, benchmarking, and challenges of electrochemical reduction of CO_2 by molecular catalysts, Adv. Energy Mater. 9 (2019) 1900090.
[13] R. Francke, B. Schille, M. Roemelt, Homogeneously catalyzed electroreduction of carbon dioxide-methods, mechanisms, and catalysts, Chem. Rev. 118 (2018) 4631–4701.
[14] X. Huang, Y.-B. Zhang, Reticular materials for electrochemical reduction of CO_2, Coord. Chem. Rev. 427 (2021) 213564.
[15] C.S. Diercks, Y. Liu, K.E. Cordova, O.M. Yaghi, The role of reticular chemistry in the design of CO_2 reduction catalysts, Nat. Mater. 17 (2018) 301–307.
[16] Y. Wang, Y. Li, Z. Wang, P. Allan, F. Zhang, Z. Lu, Reticular chemistry in electrochemical carbon dioxide reduction, Sci. China Mater. 63 (2020) 1113–1141.
[17] Y. Wu, S. Cao, J. Hou, Z. Li, B. Zhang, P. Zhai, et al., Rational design of nanocatalysts with nonmetal species modification for electrochemical CO_2 reduction, Adv. Energy Mater. 10 (2020) 2000588.
[18] D. Gao, R.M. Arán-Ais, H.S. Jeon, B. Roldan Cuenya, Rational catalyst and electrolyte design for CO2 electroreduction towards multicarbon products, Nat. Catal. 2 (2019) 198–210.
[19] Y. Lu, W. Chen, Sub-nanometre sized metal clusters: from synthetic challenges to the unique property discoveries, Chem. Soc. Rev. 41 (2012) 3594–3623.
[20] X. Zhao, X. Kong, F. Wang, R. Fang, Y. Li, Metal sub-nanoclusters confined within hierarchical porous carbons with high oxidation activity, Angew. Chem. Int. Ed. 60 (2021) 10842–10849.
[21] L. Liu, A. Corma, Confining isolated atoms and clusters in crystalline porous materials for catalysis, Nat. Rev. Mater. 6 (2021) 244–263.
[22] C. Dong, Y. Li, D. Cheng, M. Zhang, J. Liu, Y.-G. Wang, et al., Supported metal clusters: fabrication and application in heterogeneous catalysis, ACS Catal. 10 (2020) 11011–11045.
[23] Z. Jiang, X. Xu, Y. Ma, H.S. Cho, D. Ding, C. Wang, et al., Filling metal-organic framework mesopores with TiO_2 for CO_2 photoreduction, Nature 586 (2020) 549–554.
[24] J. Liu, W. Shi, B. Ni, Y. Yang, S. Li, J. Zhuang, et al., Incorporation of clusters within inorganic materials through their addition during nucleation steps, Nat. Chem. 11 (2019) 839–845.
[25] Y. Jiang, Y. Yu, X. Zhang, M. Weinert, X. Song, J. Ai, et al., N-heterocyclic carbene-stabilized ultrasmall gold nanoclusters in a metal-organic framework for photocatalytic CO_2 reduction, Angew. Chem. Int. Ed. 60 (2021) 17388–17393.
[26] R. Ye, A.V. Zhukhovitskiy, C.V. Deraedt, F.D. Toste, G.A. Somorjai, Supported dendrimer-encapsulated metal clusters: toward heterogenizing homogeneous catalysts, Acc. Chem. Res. 50 (2017) 1894–1901.
[27] C.S. Diercks, O.M. Yaghi, The atom, the molecule, and the covalent organic framework, Science 355 (2017) eaal1585.
[28] N. Huang, P. Wang, D. Jiang, Covalent organic frameworks: a materials platform for structural and functional designs, Nat. Rev. Mater. 1 (2016) 16068.
[29] J. Jiang, Y. Zhao, O.M. Yaghi, Covalent chemistry beyond molecules, J. Am. Chem. Soc. 138 (2016) 3255–3265.
[30] M. Lu, M. Zhang, J. Liu, Y. Chen, J.-P. Liao, M.-Y. Yang, et al., Covalent organic framework based functional materials: important catalysts for efficient CO_2 utilization, Angew. Chem. Int. Ed. 61 (2022) e202200003.
[31] Y. Liu, W. Zhou, W.L. Teo, K. Wang, L. Zhang, Y. Zeng, et al., Covalent-organic-framework-based composite materials, Chem 6 (2020) 3172–3202.
[32] Y. Deng, Z. Zhang, P. Du, X. Ning, Y. Wang, D. Zhang, et al., Embedding ultrasmall au clusters into the pores of a covalent organic framework for enhanced photostability and photocatalytic performance, Angew. Chem. Int. Ed. 59 (2020) 6082–6089.
[33] M. Lu, M. Zhang, J. Liu, T.-Y. Yu, J.-N. Chang, L.-J. Shang, et al., Confining and highly dispersing single polyoxometalate clusters in covalent organic frameworks by covalent linkages for CO_2 photoreduction, J. Am. Chem. Soc. 144 (2022) 1861–1871.
[34] K. Gottschling, G. Savasci, H. Vignolo-Gonzalez, S. Schmidt, P. Mauker, T. Banerjee, et al., Rational design of covalent cobaloxime-covalent organic framework hybrids for enhanced photocatalytic hydrogen evolution, J. Am. Chem. Soc. 142 (2020) 12146–12156.
[35] S. Lin, C.S. Diercks, Y.-B. Zhang, N. Kornienko, E.M. Nichols, Y. Zhao, et al., Covalent organic frameworks comprising cobalt porphyrins for catalytic CO_2 reduction in water, Science 349 (2015) 1208.
[36] M. Lu, J. Liu, Q. Li, M. Zhang, M. Liu, J.-L. Wang, et al., Rational design of crystalline covalent organic frameworks for efficient CO_2 photoreduction with H_2O, Angew. Chem. Int. Ed. 58 (2019) 12392–12397.
[37] B. Zhang, M. Wei, H. Mao, X. Pei, S.A. Alshmimri, J.A. Reimer, et al., Crystalline dioxin-linked covalent organic frameworks from irreversible reactions, J. Am. Chem. Soc. 140 (2018) 12715–12719.
[38] X. Guan, H. Li, Y. Ma, M. Xue, Q. Fang, Y. Yan, et al., Chemically stable polyarylether-based covalent organic frameworks, Nat. Chem. 11 (2019) 587–594.
[39] M. Lu, M. Zhang, C.-G. Liu, J. Liu, L.-J. Shang, M. Wang, et al., Stable dioxin-linked metallophthalocyanine covalent organic frameworks (COFs) as photo-coupled electrocatalysts for CO_2 reduction, Angew. Chem. Int. Ed. 60 (2021) 4864–4871.
[40] Y. Wang, Z. Chen, P. Han, Y. Du, Z. Gu, X. Xu, et al., Single-atomic Cu with multiple oxygen vacancies on ceria for electrocatalytic CO_2 reduction to CH_4, ACS Catal. 8 (2018) 7113–7119.
[41] J. Jiao, R. Lin, S. Liu, W.-C. Cheong, C. Zhang, Z. Chen, et al., Copper atom-pair catalyst anchored on alloy nanowires for selective and efficient electrochemical reduction of CO_2, Nat. Chem. 11 (2019) 222–228.
[42] J.H. Zhou, K. Yuan, L. Zhou, Y. Guo, M.Y. Luo, X.Y. Guo, et al., Boosting electrochemical reduction of CO_2 at a low overpotential by amorphous Ag-Bi-S-O decorated Bi0 nanocrystals, Angew. Chem. Int. Ed. 131 (2019) 14335–14339.
[43] X. Liu, J. Xiao, H. Peng, X. Hong, K. Chan, J.K. Nørskov, Understanding trends in electrochemical carbon dioxide reduction rates, Nat. Commun. 8 (2017) 15438.
[44] Q. Hu, Z. Han, X. Wang, G. Li, Z. Wang, X. Huang, et al., Facile synthesis of sub-nanometric copper clusters by double confinement enables selective reduction of carbon dioxide to methane, Angew. Chem. Int. Ed. 59 (2020) 19054–19059.
[45] Y. Cai, J. Fu, Y. Zhou, Y.-C. Chang, Q. Min, J.-J. Zhu, et al., Insights on forming N,O-coordinated Cu single-atom catalysts for electrochemical reduction CO_2 to methane, Nat. Commun. 12 (2021) 586.
[46] M. Li, Y. Ma, J. Chen, R. Lawrence, W. Luo, M. Sacchi, et al., Residual chlorine induced cationic active species on a porous copper electrocatalyst for highly stable electrochemical CO_2 reduction to C_{2+}, Angew. Chem. Int. Ed. 60 (2021) 11487–11493.
[47] H. Xu, Y. Ma, J. Chen, W.-x. Zhang, J. Yang, Electrocatalytic reduction of nitrate-a step towards a sustainable nitrogen cycle, Chem. Soc. Rev. 51 (2022) 2710–2758.
[48] F. Zhang, J. Chen, J. Yang, Fiber materials for electrocatalysis applications, Adv. Fiber Mater. 4 (2022) 720–735.
[49] D.M. Weekes, D.A. Salvatore, A. Reyes, A. Huang, C.P. Berlinguette, Electrolytic CO_2 reduction in a flow cell, Acc. Chem. Res. 51 (2018) 910–918.
[50] Z.-Z. Niu, L.-P. Chi, R. Liu, Z. Chen, M.-R. Gao, Rigorous assessment of CO_2 electroreduction products in a flow cell, Energy Environ. Sci. 14 (2021) 4169–4176.
[51] X. Nie, M.R. Esopi, M.J. Janik, A. Asthagiri, Selectivity of CO_2 reduction on copper electrodes: the role of the kinetics of elementary steps, Angew. Chem. Int. Ed. 52 (2013) 2459–2462.
[52] A.A. Peterson, F. Abild-Pedersen, F. Studt, J. Rossmeisl, J.K. Nørskov, How copper catalyzes the electroreduction of carbon dioxide into hydrocarbon fuels, Energy Environ. Sci. 3 (2010) 1311–1315.
[53] S. Kattel, W. Yu, X. Yang, B. Yan, Y. Huang, W. Wan, et al., CO_2 hydrogenation over oxide-supported PtCo catalysts: the role of the oxide support in determining the product selectivity, Angew. Chem. Int. Ed. 55 (2016) 7968–7973.
[54] L. Wang, L. Wang, J. Zhang, X. Liu, H. Wang, W. Zhang, et al., Selective Hydrogenation of CO_2 to ethanol over cobalt catalysts, Angew. Chem. Int. Ed. 57 (2018) 6104–6108.
[55] N.J. Firet, W.A. Smith, Probing the Reaction Mechanism of CO_2 electroreduction over Ag films via operando infrared spectroscopy, ACS Catal. 7 (2017) 606–612.
[56] J.-D. Yi, R. Xie, Z.-L. Xie, G.-L. Chai, T.-F. Liu, R.-P. Chen, et al., Highly selective CO_2 electroreduction to CH_4 by in situ generated Cu_2O single-type sites on a conductive mof: stabilizing key intermediates with hydrogen bonding, Angew. Chem. Int. Ed. 59 (2020) 23641–23648.
[57] M. Elavarasan, W. Yang, S. Velmurugan, J.-N. Chen, Y.-T. Chang, T.C.-K. Yang, et al., In-situ infrared investigation of m-TiO_2/α-Fe_2O_3 photocatalysts and tracing of intermediates in photocatalytic hydrogenation of CO_2 to methanol, J. CO2 Util. 56 (2022) 101864.